
Article:
Silva, S.S.A., Verth, G., Rempel, E.L. et al. (3 more authors) (2021) Solar vortex tubes. II. On the origin of magnetic vortices. The Astrophysical Journal, 915 (1). 24. ISSN 0004-637X

https://doi.org/10.3847/1538-4357/abfec2

Draft version September 23, 2021
Typeset using LaTeX default style in AASTeX63

Solar Vortex Tubes II: On the origin of magnetic vortices

Suzana S. A. Silva [1,2] Gary Verth,[3] Erico L. Rempel,[4] Sergiy Shelyag,[5] Luiz A. C. A. Schiavo,[6] and Viktor Fedun[1]

[1] *Plasma Dynamics Group, Department of Automatic Control and Systems Engineering, University of Sheffield, Sheffield, UK*
[2] *Department of Physics, Aeronautics Institute of Technology, São José dos Campos, Brazil*
[3] *Plasma Dynamics Group, School of Mathematics and Statistics, University of Sheffield, Sheffield, UK*
[4] *Department of Mathematics, Aeronautics Institute of Technology, São José dos Campos, Brazil*
[5] *School of Information Technology, Deakin University, Geelong, Australia*
[6] *São Paulo State University (UNESP), São João da Boa Vista, Brazil*

Submitted to ApJ

ABSTRACT

The solar atmosphere presents a wealth of dynamics due to a constant interplay between the plasma flows and magnetic fields. Twisted flux tubes are an essential magnetic structure, believed to be driven by rotational surface's motions and linked to plasma heating, jets and eruptive phenomena. Despite extensive investigations, twisted magnetic flux tubes lack a proper mathematical definition, precluding their automatic detection. This work addresses this issue by defining them as magnetic vortices and introduces a formal definition which is based on a recently developed magnetic vortices detection technique, the Integrated Averaged Current Deviation method. We applied this method and kinetic vortices identification technique to realistic magneto-convection simulations obtained from the MURaM code. The preferential site for these two types of vortices is the intergranular downflow, but while the magnetic vortices are found mostly in the small areas where plasma-$\beta > 1$, the rotational flow structures, the kinetic vortices, were detected in locations where plasma-$\beta < 1$. The magnetic vortices locally concentrate the magnetic field's vertical components and current, lasting on average around a minute. Two types of magnetic vortices are introduced based on their magnetic to kinetic energy ratio. For the first type, the magnetic energy prevails, and the magnetic vortices are mostly vertical. The second type of magnetic vortices presents distinct shapes and a lower magnetic to kinetic energy ratio. We have found that magnetic vortices may appear if two conditions are simultaneously present: (i) shear flow, (ii) plasma-$\beta > 1$. The presence of rotational motion is not necessary.

1. INTRODUCTION

The quiet Sun is characterised by a wide variety of plasma flows which are believed to determine the distribution (Chian et al. 2019), concentration (Requerey et al. 2018) and topology of magnetic fields. Swirling patterns are spread in plasma flows along intergranular lanes as found both by observations (Bonet et al. 2008; Balmaceda et al. 2010; Bonet et al. 2010) and realistic magneto-convection simulations (Shelyag et al. 2011; Moll et al. 2012; Shelyag et al. 2013; Kato & Wedemeyer 2017). Both simulations and observations support that solar vortices are three-dimensional vertical structures connecting the lower photosphere to the upper chromosphere (Wedemeyer-Böhm et al. 2012; Kitiashvili et al. 2012a, 2013; Silva et al. 2020; Yadav et al. 2021), channeling enough energy to heat the chromosphere (Shelyag et al. 2012; Yadav et al. 2021). These solar vortex tubes concentrate the magnetic fluxes in their interior, leading to plasma dynamics inside the tubes to be more strongly impacted by the Lorentz force (Kitiashvili et al. 2013; Silva et al. 2020). The interaction of vortex plasma flows with the turbulent magnetic flux found in the downflow organize and create new magnetic structures (Snow et al. 2018). In particular, it is believed that those surface rotational motions are able to twist the magnetic field lines in regions where the atmosphere is not dominated by magnetic pressure, which

Corresponding author: Suzana S. A. Silva
suzana.seas@gmail.com

would allow the magnetic field lines to be easily carried by the plasma. This poses the photospheric solar vortices as potential drivers to create twisted magnetic flux tubes. This role has been exploited in several papers, (e.g. Fedun et al. 2011a; Mumford et al. 2015). In turn, in the upper part of the atmosphere where the magnetic field rules the dynamics, twisted flux tubes may drive rotational motions along the magnetic field lines, which would be observed as dark rings in Hα and Ca II line core, the so-called chromospheric swirls (Wedemeyer-Böhm & Rouppe van der Voort 2009). Those rotating chromospheric structures can be be short (Shetye et al. 2019) or long-lived (Tziotziou et al. 2018) and they tend to be dominated by not only rotation, but also swaying motions (Tziotziou et al. 2019) related to alfvenic waves (Tziotziou et al. 2020). Yadav et al. (2021) proposed that due to turbulence, large chromospheric swirls cascade down to smaller-scale vortices inside magnetic elements and align to the magnetic field lines. Another important dynamical feature of twisted magnetic flux tubes is the generation of a Lorentz force which leads to jet-like behaviour in the chromospheric part of simulated atmospheres (Kitiashvili et al. 2013; Iijima & Yokoyama 2017) and torsional wave excitation, e.g (Vasheghani Farahani, S. et al. 2017; Ebadi et al. 2021).

Up to now, only a few studies have addressed the impact of spontaneously generated vortex tubes in the shaping of magnetic flux tubes. Investigations based on data from realistic solar atmospheric models conclude that the vortices can create bending vertical magnetic flux tubes, but there seems to be no significant twist to most vortices (Moll et al. 2012; Shelyag et al. 2013; Silva et al. 2020). Kitiashvili et al. (2013) and Silva et al. (2020) found instances of kinetic vortices encompassing weak magnetic field regions where the magnetic field lines were twisted and, in their analysis, the twisting occurred in the opposite direction of the vortex rotation. The absence of robust numerical studies concerning kinetic vortices' fundamental role in creating twisted flux tubes is a consequence of lacking a proper definition for those magnetic structures and an automatic method to detect them in complex flows. This paper proposes to broaden the solar vortex typology and define the twisted flux tube as a vortex where the twist is observed in the magnetic field. Thereby, we name such structures magnetic vortices, and we introduce a formal definition that enables a proper three-dimensional vortex identification. Both the vortex definition and detection are based on a recently developed method to detect magnetic vortex boundaries which precisely defines the region where the magnetic field lines have the topology of a magnetic flux tube (Rempel et al. 2017, 2019). We apply kinetic and magnetic vortex detection methods to realistic radiative magneto-convection simulations and analyze the plasma within magnetic vortices and those structures' lifetime. Finally, we present a flow analysis to address the matter of the creation of twisted flux tubes. This work is organized as follows: the magnetic vortex definition and detection method are presented in Section 2; the magnetic vortex distribution, lifetime, and radial profiles in Section 3; the types of magnetic vortex are introduced in section 4; an analysis of the plasma flow driving the magnetic vortices is given in Section 4; and, lastly, conclusions and discussions of our findings are presented in Section 6.

2. METHODOLOGY

We used a sequence of time frames obtained from a magneto-convection simulation performed by the MURaM code to detect and analyze magnetic vortices, i.e., bounded coherent sets of twisted magnetic field lines. Thereby, we are interested in identifying regions where the magnetic field presents an organized twisted coherent flux tube in a simulated atmosphere. The simulation domain covers 24×24 Mm in the horizontal directions and 1.6 Mm in the vertical direction. The visible solar surface is located around $z = 1$ Mm, which is 600 km below the upper boundary. Further information on the code and this simulation in particular can be found in Vögler et al. (2005) and Silva et al. (2020), respectively. We analyzed the central region of the domain which covers 12x12 Mm in the horizontal plane. Figure 1 shows the vertical component of the velocity field for a xy-plane placed at $z = 1.0$ Mm. The domain analyzed in this paper is delimited by a cyan square, 12x12 Mm. The black dashed square, 6x6 Mm, shows the part of the domain used to produce close view figures of our results throughout our analysis. Also, for our analysis we considered cgs units. Thereby, unless stated otherwise, all the units in the Figures are in cgs"

For conciseness, from this point on we will refer to magnetic vortices as M-vortices and kinetic vortices as K-vortices. In order to define the M-vortex, we propose a two-step method where we first identify the vortex's center and next we define the vortex's boundary. For the center detection, we require an M-vortex to be a magnetic structure which continuously curls around its center along a given plane as indicated in Fig. 2. The M-vortex center can be automatically detected by using the d-parameter from Silva et al. (2018) with the displacement replaced by the magnetic field components in a given plane. Therefore, we applied a geometrical analysis of the horizontal components of the magnetic field by checking, for each grid point, if the orientation of the field at four nearest neighbouring points indicates that it curls around that grid point as explained by Silva et al. (2018). The left panel of Fig. 2 shows the

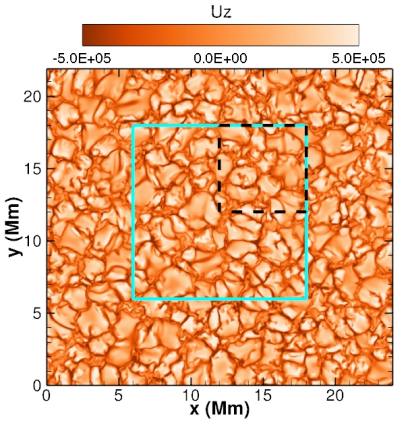

Figure 1. Simulation domain 2D view: The xy-plane of the whole domain at $z = 1.0$ Mm colored by the z-component of the velocity. The part of the domain investigated in this paper is delimited by a cyan square.The dashed black square delimits the region used to plot 3D and 2D images of the domain.

magnetic field lines for a magnetic structure presenting a swirling pattern in the horizontal plane. The blue arrows on the planes in the right panels represent the horizontal component, $\mathbf{B}_h$, of the magnetic field. The field lines are twisted along a vertical length of 0.2 Mm just above the solar surface, and we see that the center of the curling pattern presents a local concentration of vertical current created by the twisting of the magnetic flux tube. Next, we

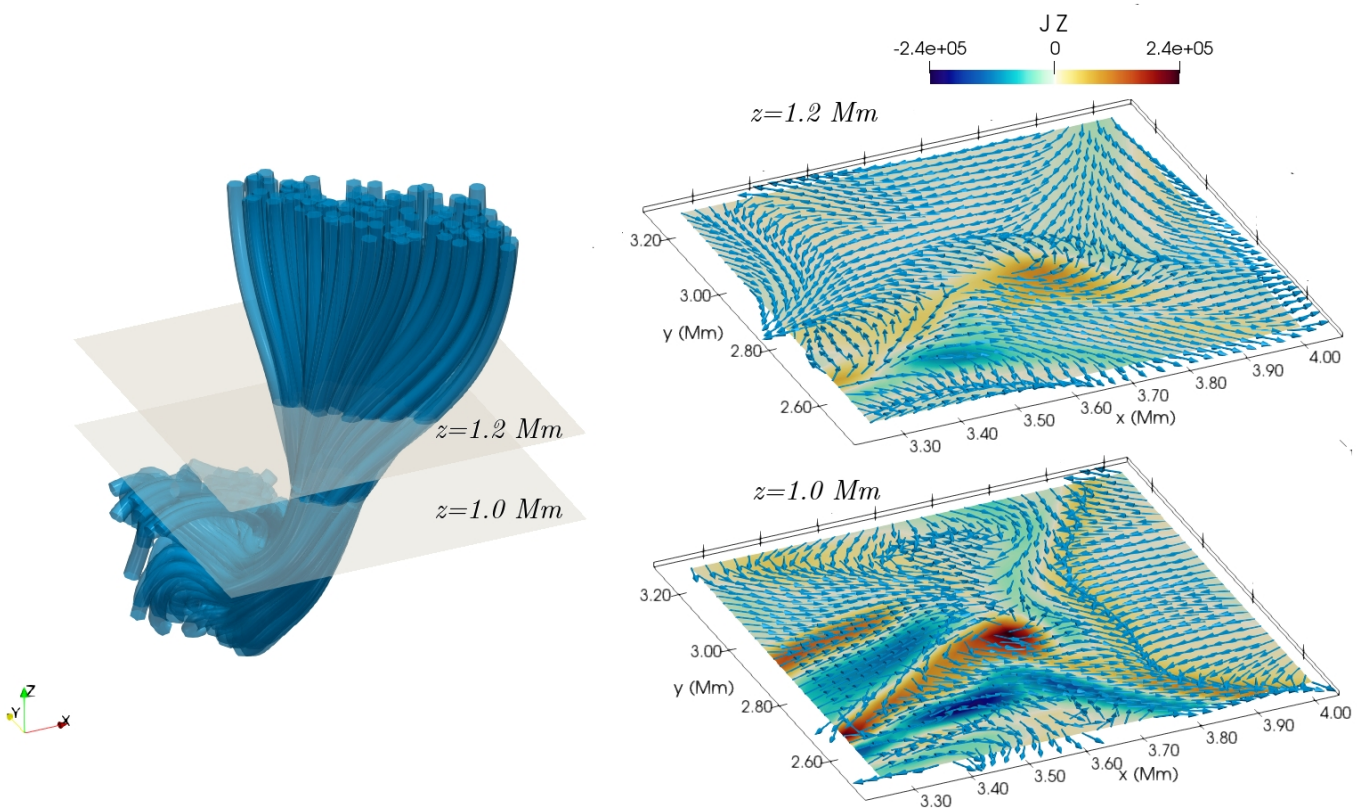

Figure 2. Left panel: The magnetic field lines for an M-vortex are represented by blue tubes. The two xy-planes, placed at $z = 1$ Mm and $z = 1.2$ Mm and colored in light khaki, represent the slices portrayed in the right lower panel and the right upper panel, respectively. Right panel: Slices colored by the z-component of the current density, $\mathbf{J}$, with arrows in blue showing the orientation of the horizontal components of the magnetic field.

define the M-vortex boundary by identifying the region where the topology of magnetic field lines defines a coherent

twisted magnetic flux tube. Defining of M-vortex as a coherent structure of the magnetic field can be done using the Instantaneous Averaged Current Deviation (IACD) method (Rempel et al. 2019). The IACD field is defined as

$$\mathrm{IACD}_{s_0}^{s_0+\xi}(\mathbf{x_0}, t) := \int_{s_0}^{s_0+\xi} |\mathbf{J}(\mathbf{x}(s), t) - \langle \mathbf{J}(t) \rangle| ds, \tag{1}$$

where $\mathbf{J} = \frac{c}{4\pi} \nabla \times \mathbf{B}$ is the current density computed for a time t_0 at a position defined by the vector $\mathbf{x}$; c is the speed of light, and $\langle \cdot \rangle$ denotes the instantaneous spatial average. Integration is along a magnetic field line, starting at the position defined by $\mathbf{x_0}$ and ds is an arc-length differential parameter. The length of the integration, ξ, is chosen as a characteristic scale along the field line for which the structures sought are expected to remain coherent and should be chosen empirically. The M-vortex boundary on a horizontal plane is defined as the outermost convex closed contour of the IACD field around the spiralling center given by the magnetic d-parameter. Thus, we analyze the convexity of countour lines around the center and choose the outermost convex curve. Closed contours are considered convex if their deviation from convexity is below a certain threshold. The deviation from convexity is defined as:

$$\epsilon = \frac{A_c - A_{ch}}{A_c}, \tag{2}$$

where A_c is the area of the region enclosed by the extracted contour and A_{ch} is the area enclosed by its convexhull. For this particular MURaM simulation, contour lines are considered convex if $\epsilon \leq 0.009$.

From Eq. 1, we have that different values for the length of integration will lead to different M-vortex boundaries. The choice for ξ depends on the problem under consideration, and as we are interested in finding structures that can reach the upper part of the domain, we consider that the M-vortex should remain coherent for the vertical extent of the domain above the approximate solar surface. Thus, we computed the IACD field for each xy-plane in the range 1 Mm $\leq z \leq$ 1.4 Mm. For each horizontal plane, the value of ξ was defined as the distance from that given plane to the plane $z = 1.5$ Mm. We exclude the upper 100 km of the domain from the analysis as the amount of twist in that height range tends to be low, for it is too close to the upper boundary, where the magnetic field is forced to be vertical.

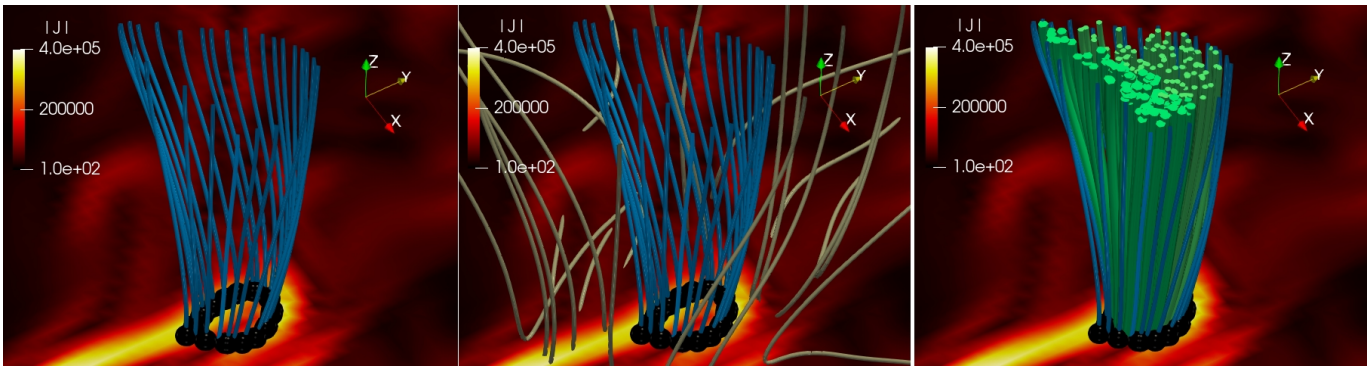

Figure 3. The vortex boundary of an M-vortex as defined by IACD for $\xi = 0.48$ Mm. The xy-plane is placed at $z = 1.2$ Mm and it is colored by the magnitude of the current. The magnetic field lines are shown in blue for lines traced from the boundary, in gray for lines traced from outside the M-vortex (middle panel) and in green (right panel) for lines traced from points inside the M-vortex.The M-vortex has a radius around 60 km and the blue magnetic lines reach the upper part of the domain, z=1.6 Mm.

The meaning of the vortex boundary defined by IACD is illustrated in Fig. 3. The black spheres represent points along the boundary of a M-vortex detected by IACD in the xy-plane at $z = 1.02$ Mm, where we detected this vortex's lower base. The horizontal plane is coloured by the magnitude of the current density and the magnetic field lines traced from the vortex boundary are shown in blue whereas the ones traced outside the boundary are shown in grey (middle panel), and the green lines are traced from points inside the M-vortex. The boundary delimits a region where the vortex boundary lines are twisted and preserve their coherence for the length used to compute the IACD field. The magnetic field lines inside the vortex are also twisted, forming a coherent twisted flux tube.

The vortex boundary lies close to a region of local maxima of the current density magnitude, but is not perfectly aligned with it, as the current density was computed only on the plane, whereas the IACD field considers the current

density integrated along the field lines, away from the plane. Therefore, working only with the current magnitude in a plane to detected coherent flux tubes may yield poor results. In fact, the magnetic field lines traced from seed points just outside the vortex boundary present dispersed field lines, even when they are traced from seed points located in the high current region. This demonstrates the IACD method's precision to detect twisted magnetic flux tubes, even in regions filled with jumbled magnetic field lines as here. The lines traced from points inside the M-vortex (green lines) do not cross the vortex boundary (blue lines). Therefore, IACD provides a proper physical definition for twisted magnetic flux tubes and allows automatic detection of those structures.

3. RESULTS

We computed the densities of M- and K-vortices in the domain, i.e., the number of three-dimensional vortices per Mm^2. The densities of $\sim 13/\mathrm{Mm}^2$ and $\sim 28/\mathrm{Mm}^2$ were detected for M- and K-vortices, respectively. These values were computed by averaging detections over a time period of 500s. For some vortices, the rotation of magnetic components occurs within only a small height range, whereas for other vortices the spiraling pattern is observed up to a half of the analyzed planes. On average, the lower part of the vortex is found at $z = 1.06$ Mm. In other words, most of the detected coherent M-vortices are twisted at a height 60 km above the solar surface. The K-vortices were detected using the Instantaneous Vorticity Deviation (IVD) method (Haller et al. 2016):

$$\mathrm{IVD}(\mathbf{x}, t) := |\omega(\mathbf{x}, t) - \langle\omega(t)\rangle|, \tag{3}$$

where $\mathbf{x}$ is a position vector, $\omega = \nabla \times \mathbf{U}$ is the vorticity, $\mathbf{U}$ is the velocity field, and $\langle\cdot\rangle$ denotes the instantaneous spatial average at time t. Similarly to IACD, IVD was computed for each plane above the solar surface. Further details on the construction of 3D K-vortex tubes can be found in Silva et al. (2020). Figure 4 displays the magnetic field lines of all detected magnetic vortices represented by white lines. The red lines show the velocity field streamlines from detected K-vortices. In the intergranular downflow, there is a competition between the Lorentz force and pressure gradients to govern the plasma dynamics, as indicated by the different values of the plasma-β found in the region. The K-vortices are located in low plasma-β regions, and the M-vortices are present in regions of the flow with higher plasma-β.

Figure 5(a) depicts the magnetic field lines delimiting the boundary for an M-vortex placed on a xy-plane at $z = 1.05$ Mm, colored by $\log\beta$. The field lines are also immersed in the volume rendering of the $\log\beta$. The region encompassed by the vortex has a positive value for $\log\beta$, which tends to be greater than zero and closer to one in the region where the twist occurs. This is confirmed by the average radial profile for $\log\beta$ (Figure 5(b)), which was averaged for all M-vortices. Therefore, M-vortices appear in regions of the flow where the dynamics are ruled by hydrodynamics, whereas the magnetic field strongly impacts the K-vortices' plasma dynamics.

In Fig. 6, the distribution of the detected magnetic vortices is shown in more detail for M-vortices detected in the range 1 Mm $\leq z \leq$ 1.1 Mm. The black lines denote the boundaries of vortices. The horizontal cuts of the plasma parameters are taken at $z = 1$ Mm. Figure 6(a) shows the horizontal plane coloured by the z-component of the velocity field and confirms M-vortices' preferential locations, the downflow regions. This is expected since our computation favours detecting the vertical coherent structures which, in turn, are found in the intergranular downflows. On the other hand, magnetic vortices do not tend to appear in regions with strong magnetic field concentrations, Fig. 6(b), as it would be tough to twist the magnetic field lines, especially as plasma-β goes lower as depicted in Fig. 6(c). As the magnetic field lines are twisted, the M-vortices are mostly found at high current density regions as shown in Fig. 6(d) for the magnitude of current and in Fig. 6(e) for the z-component of the current.

3.1. *Lifetime and Radial Profiles*

We carried out statistical analysis of the vortex population to investigate the average lifetime of such events. The vortex-tracking across different time frames was based on average behavior of the vortex centers in the domain at some randomly selected times. Such analysis provided the parameters used to consider two structures at different time frames as the same coherent vortex. First, we noticed that the minimal spatial distance between two vortex centers was greater than four grid points and that also new vortices never appear next to an existing vortex within that length. Therefore, any two structures identified at consecutive frames within that spatial distance were considered to be the same vortex. Tests carried out using advection of magnetic field lines, or advection of particles in the flow confirmed that our analysis parameters allow the temporal identification of vortices. Figure 7 shows histograms of the lifetime of vortices that have vertical length greater or equal to 0.1 Mm. Figures 7(a) and Figure 7(b) show the lifetime distribution for the M-vortex and the K-vortex populations, respectively. We can see that K-vortices have a

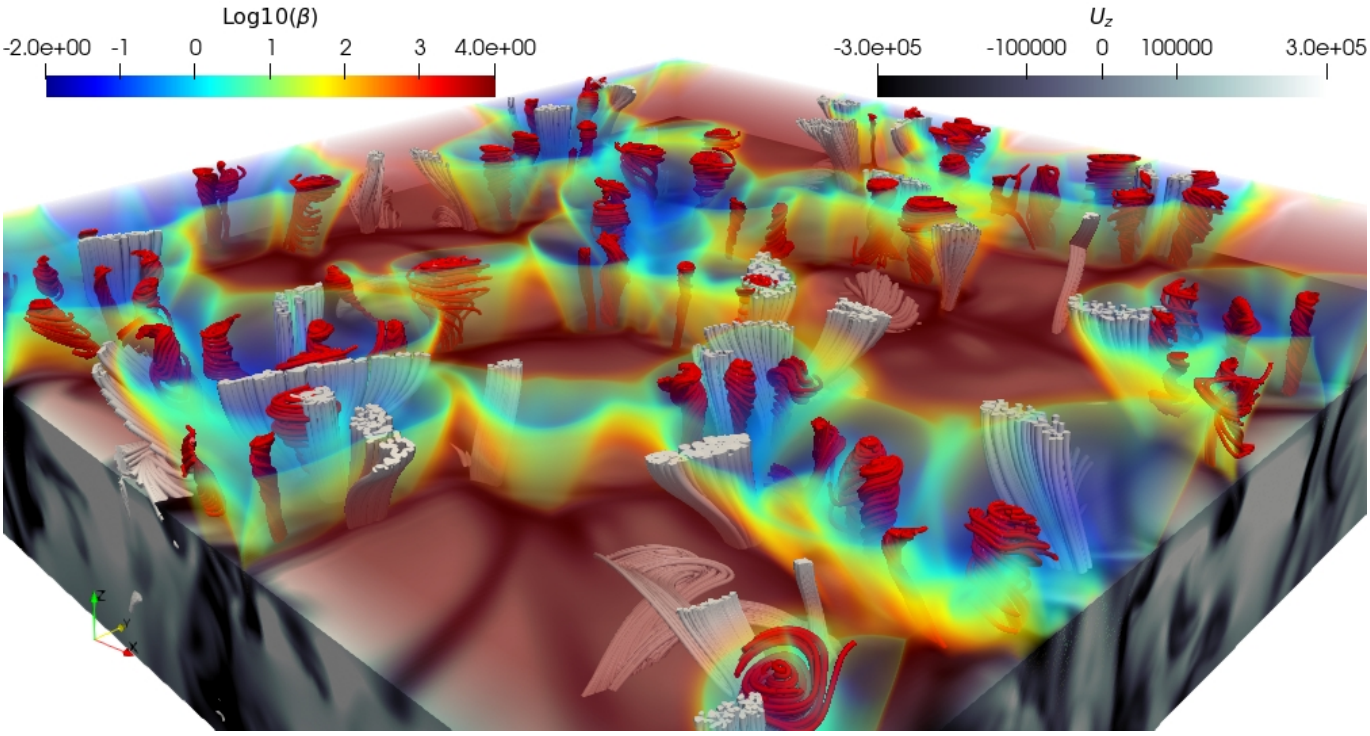

Figure 4. Three-dimensional view of part of the analyzed domain, 6x6x1.6 Mm with the volume rendering of the logarithm of the plasma beta. The magnetic (velocity) field lines are colored in blue (red) and are traced from random points within the magnetic (kinetic) vortices. The part of the domain below the solar surface is colored by the vertical component of the velocity field.

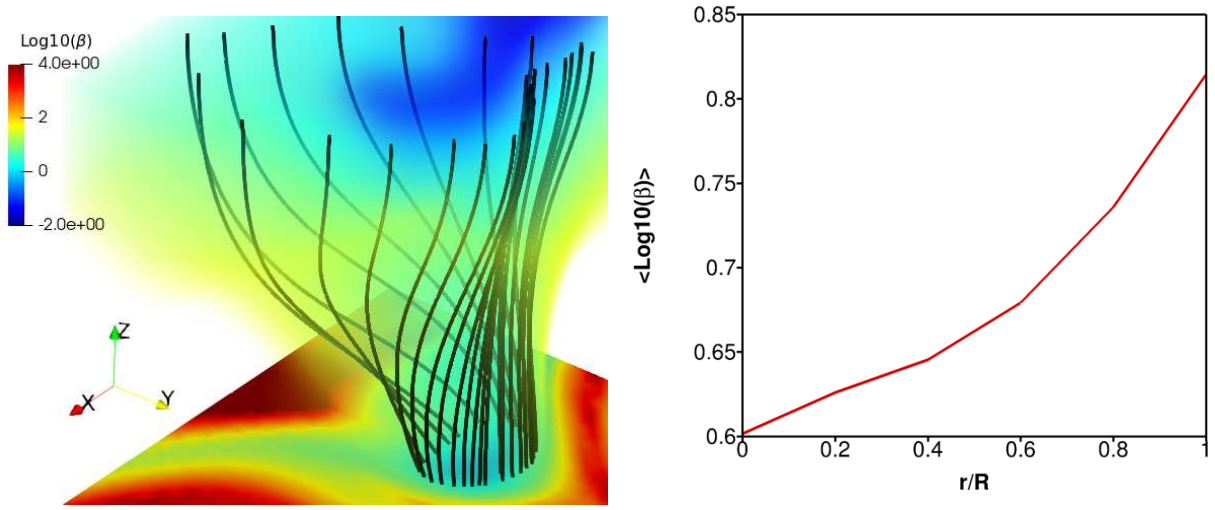

(a) (b)

Figure 5. (a) Magnetic field lines traced from an M-vortex boundary, radius $\sim$ 65 km, located in a xy-plane placed at $z = 1.05$ Mm, which is colored by the logarithm of the plasma beta. The field lines are immersed in the volume rendering of the logarithm of the plasma-β; (b) average radial profile of the logarithm of plasma-β for all detected M-vortices.

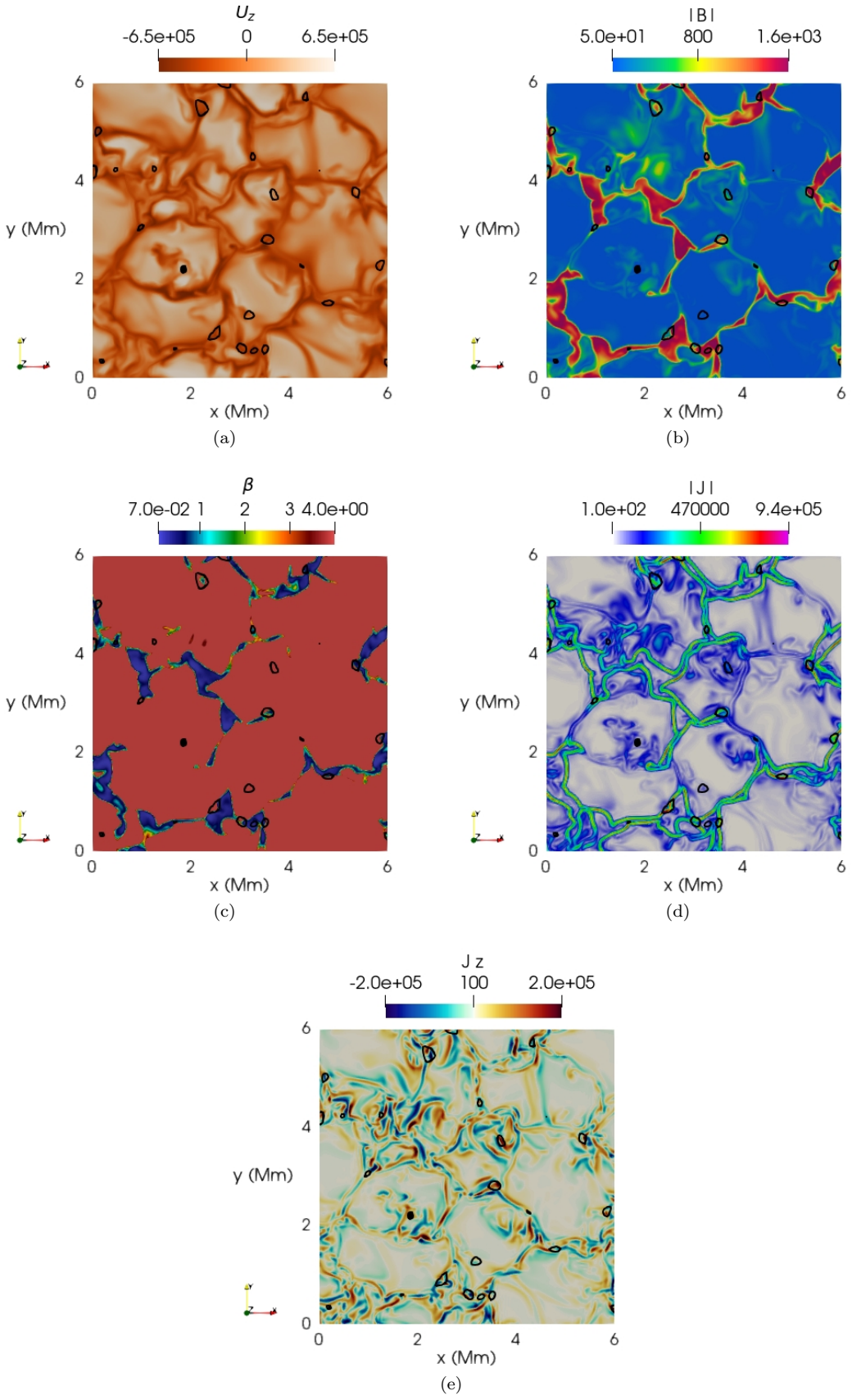

Figure 6. Detected M-vortex boundaries (black lines) for 1 Mm $\leq z \leq$ 1.1 Mm with background xy-plane placed at $z = 1$ Mm and colored by (a) the vertical component of the velocity field; (b) the magnitude of the magnetic field; (c) by the plasma-β saturated at $\beta = 4$; (d) by the current density magnitude; (e) by the vertical component of current

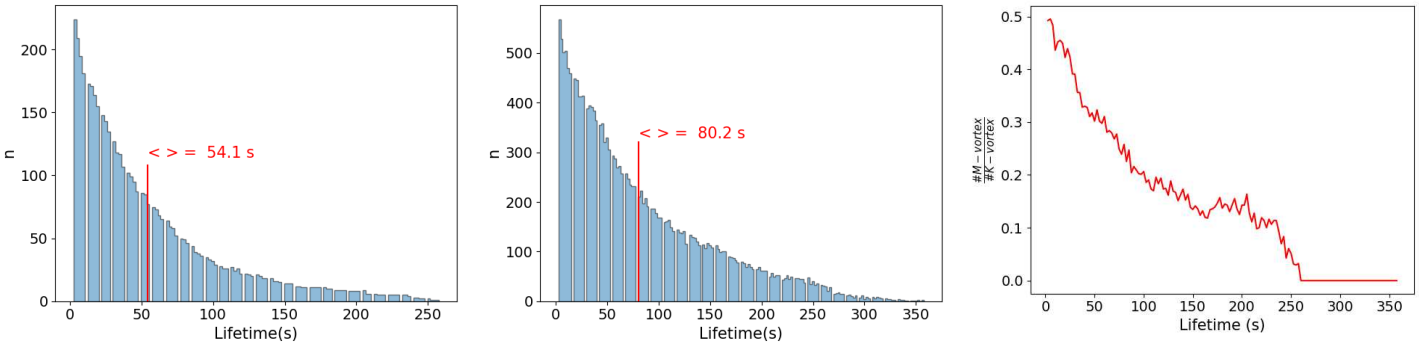

(a) M-vortices (b) K-vortices (c) Ratio

Figure 7. (a, b) Histograms of the lifetime of a vortex population with vertical length $\geq$ 0.1Mm. (a) show results for M-vortices, and (b) is for K-vortices. The red line indicates the average lifetime of the population. (c) Ratio of the total number of M-vortices and K-vortices which have the same lifetime.

mean lifetime of 84.7s, 56% longer than the M-vortices observed in the previous analysis. The histogram tail refers to events that are 3 to 4 times larger than the average lifetime observed in M- and K-vortices. Figure 7c displays the ratio of the total number of M-vortices and K-vortices with a given lifetime. We can see that there are 2 to 3 times more K-vortices in short events, up to 50s. Above 250s, no M-vortex events were observed, indicating that the flow displays more K-vortex long-duration structures than long-lived M-vortices.

The plasma properties distribution within the M-vortex can be approximated by the average radial profile. Thus, we computed the plasma variables across the magnetic vortices and averaged them along the azimuthal direction, considering a cylindrical coordinate system where the origin is placed at the vortex center detected by the d-parameter (Silva et al. 2018). Then, we averaged the height profiles for two height ranges: $1 \leq z \leq 1.1$ (Mm) and 1.3 Mm $\leq z \leq$ 1.4 Mm. The average radial profiles of magnetic vortices are shown in Fig. 8. The distribution of kinetic and

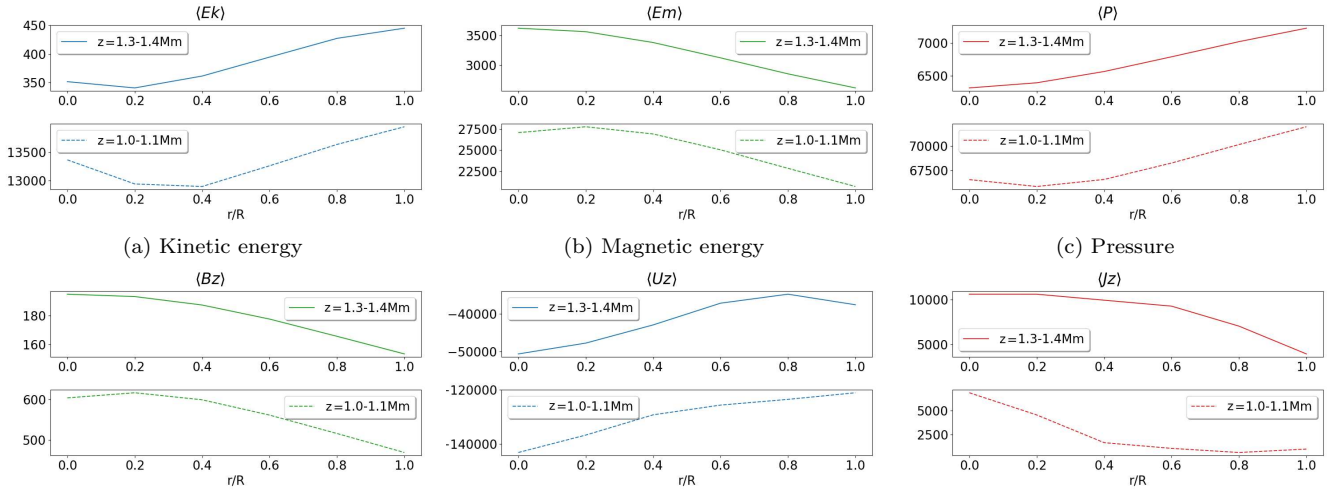

(a) Kinetic energy (b) Magnetic energy (c) Pressure

(d) Vertical magnetic field (e) Vertical velocity (f) Vertical current density

Figure 8. Averaged distribution of plasma variables along the vortex radius for all detected M-vortices. The bottom panels are for 1 Mm $\leq$z$\leq$ 1.1 Mm and the upper panels for 1.3 Mm $\leq$z$\leq$ 1.4 Mm.

magnetic energy is shown in Fig. 8(a, b). Those profiles present opposite behaviour, with the M-vortex acting as local concentration of magnetic field whereas presenting higher a kinetic energy source at its border. The gas pressure profile in Fig. 8(c) indicates that a pressure gradient exists within the M-vortex, pushing the magnetic field towards its center, explaining the radial profile for magnetic energy, Fig. 8(b), and the vertical component of the magnetic field, Fig. 8(d). The M-vortex is associated with a strong downflow of plasma in its interior at all analyzed height

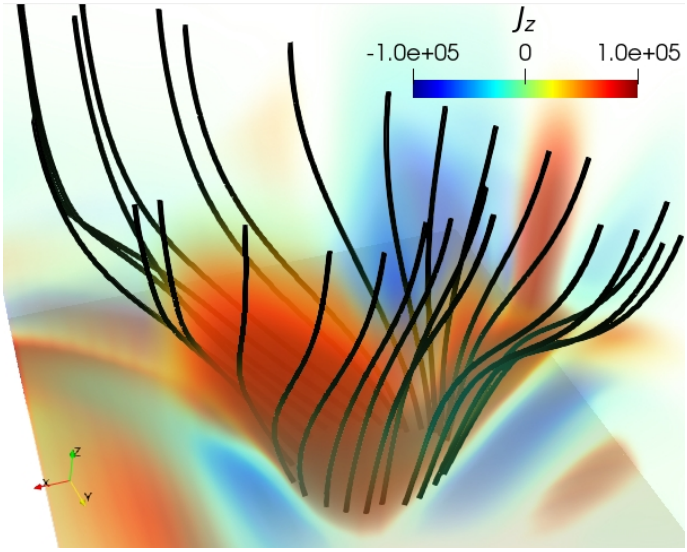

Figure 9. Magnetic field lines traced from an M-vortex boundary,, radius ~ 70 km, and embedded in the volume rendering of the vertical component of the current density.

levels, as indicated by Figure 8(e). The vertical current density field varies considerably inside the vortex, and it is concentrated at the vortex center, rapidly falling in the outward direction as displayed in Fig. 8(f). Therefore, the M-vortex presents, in general, a local concentration of vertical components of magnetic field and current. The intense concentration of J_z by M-vortices is illustrated by Fig. 9, depicting the magnetic field lines traced from an M-vortex immersed in the three-dimensional distribution of the z-component of the current density. We see that, locally, the vertical current intensifies inside the vortex, even for the higher parts of the M-vortex.

4. TYPES OF MAGNETIC VORTEX

The influence of velocity and magnetic fields for the plasma flow within the M-vortex can be evaluated by comparing the magnetic energy, E_m, and the kinetic energy, E_k, inside the vortex. Based on the ratio of magnetic and kinetic energy, we classify the M-vortices as: type I M-vortex ($E_m/E_k > 1$) and type II M-vortex ($E_m/E_k \leq 1$). Figure 10 shows the distribution of the averaged M-vortex centers (white and black circles) and K-vortex centers (blue 'X') on the xy-plane placed at $z = 1$ Mm and colour-coded by the vertical component of the velocity field. Each vortex center's average was computed considering all the xy-planes where the vortex center was detected. The circles in Fig. 10 are placed in the vortex centers and they are colored by the ratio E_m/E_k. The white circles stand for M-vortices displaying a high ratio of E_m/E_k, i.e., type I M-vortices. They are the majority and tend to be distributed along the downflow regions, where we find the higher magnetic field concentrations. The black circles denote vortices where the average kinetic energy is considerably higher than the magnetic energy. Those type II vortices correspond to around 40% of total vortices, and they tend to appear outside downflow regions, which indicates that type II vortices tend to encompass weaker magnetic field. The close view of some parts of the region shown of Fig. 10 indicates that although an M-vortex may appear close to K-vortices, they are not necessarily co-spatial. Also, M-vortices showing a higher ratio of E_m/E_k tend to appear more often closer to K-vortices than the other M-vortices.

The two types of M-vortices also show differences regarding other plasma properties as depicted in Figure 11. As before, the white circles represent the averaged center of type I and the black are for the type II. Figure 11(a) shows the distribution of the averaged M-vortex centers for $\log \beta$ for the horizontal plane at $z = 1$ Mm. We see that type II tends to be encountered in regions with a considerable higher plasma beta than type I, which in turn is mostly found in areas with unity plasma-β or transitioning from high to lower plasma-β. In other words, type I still presents some small, but significant influence from the magnetic field on the plasma dynamics, whereas in type II the plasma is mainly ruled by the gas pressure. To evaluate whether M-vortices tend to encompass compressible or incompressible plasma, we may compare the terms ruling the mass continuity equation,

$$\frac{\partial \rho}{\partial t} = -(\underbrace{\rho \nabla \cdot \mathbf{U}}_{\text{C1}} + \underbrace{(\nabla \rho) \cdot \mathbf{U}}_{\text{C2}}), \tag{4}$$

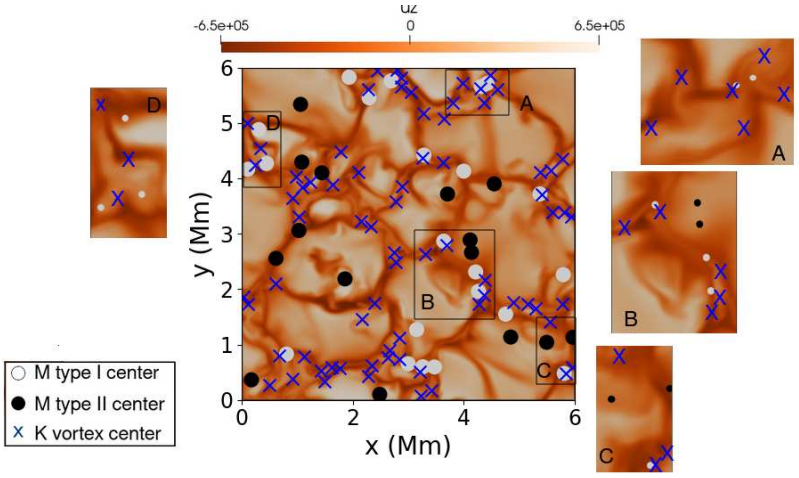

Figure 10. The xy-plane is placed at $z = 1$ Mm and is colored by the z-component of the velocity field. The circles represent the positions of the vortex centers averaged along the z-direction of each M-vortex and they are colored in white for type I M-vortices ($E_m/E_k > 1$) and in black for type II M-vortices ($E_m/E_k \leq 1$). The blue crosses represent the average centers of the K-vortices along the z-direction.

to see which one would dominate the flow. The term C1 represents the influence of fluid compressibility on the plasma dynamics. Thus, regions where $C_1/(|C_1| + |C_2|) \geq 0.5$ are the locations where compressibility is stronger in the flow. Those regions appear in hot colour in Figure 11(b) and the dark blue parts of the flow represent local regions where the plasma is approximately incompressible, since we have $C_1/(|C_1| + |C_2|) \leq 0.2$. We see that all type II vortices are in regions where compressibility effects are considerable, while the type I vortices tend to appear in areas where compressibility is more negligible for the plasma dynamics.

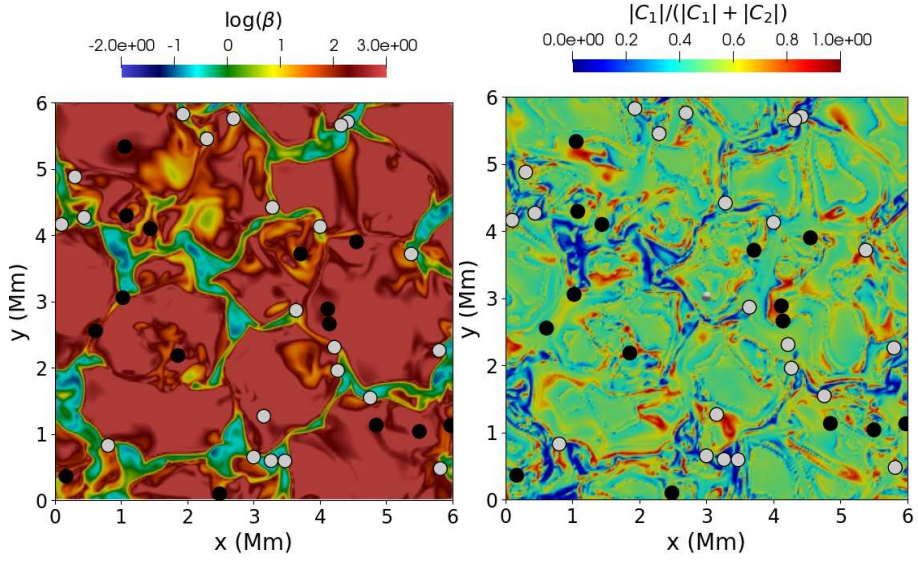

Figure 11. The circles represent the positions of the vortex centers averaged along the z-direction of each M-vortex and they are colored in white for type I M-vortices ($E_m/E_k > 1$) and in black for type II M-vortices ($E_m/E_k \leq 1$).(a) The xy-plane is placed at $z = 1$ Mm and is colored by $\log \beta$. (b) The xy-plane is placed at $z = 1$ Mm and is colored by the contribution of compressibility, $\rho \nabla \cdot \mathbf{U}$, to the mass continuity equation.

Examples of type I and type II vortices are shown in Figs. 12 and 13, respectively. The left panels in Figures 12, 13(a, b) show the magnetic field lines in blue and they are traced from random points inside the M-vortex boundary.

In the right panels, we see the instantaneous velocity field lines in red for the surrounding region. Fig. 12 shows that type I vortices have a mostly vertical geometry, and they tend to appear in regions with shear flows. In Fig. 13, we notice that type II vortices have their magnetic field lines aligned with the flow motion, indicated by the velocity field lines. Thereby, type II presents a wide variety of shapes which precludes any classification or more specific description of a general geometry.

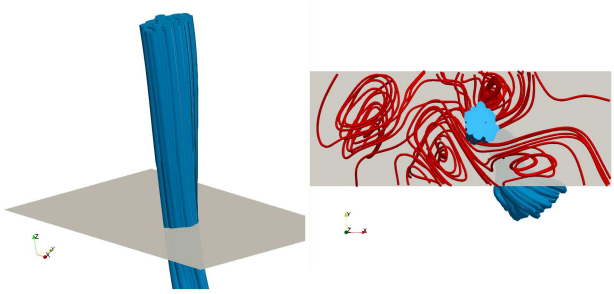

(a)

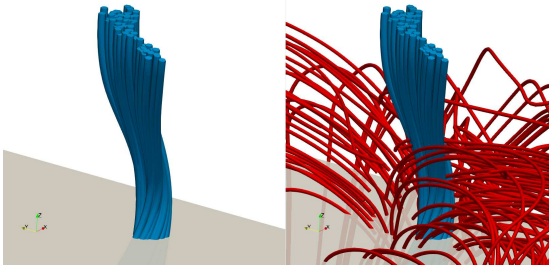

(b)

Figure 12. Left panels: an example of a type I M-vortex where the magnetic field lines are displayed in blue and are traced from random points within the M-vortex boundary, radius $\sim$ 70 km. The magnetic field lines reach the upper part of the domain, $z = 1.6$ Mm. Right panels: M-vortex magnetic field lines (blue) and the velocity field lines (red) surrounding the M-vortex. In both panels the xy-plane is placed at $z = 1$ Mm.

5. M-VORTICES AND THE PLASMA FLOW

As shown above, the magnetic and kinetic vortices tend to appear close to each other, and sometimes the rotational flow seems to encompass the twisted magnetic field lines. On the other hand, M-vortices may also appear in regions where there seem to be no K-vortices. In order to check the influence of rotation and strain on the magnetic vortices, we computed the Q-criterion,

$$Q_{crit} = \frac{1}{2}[|\overline{\mathbf{\Omega}}|^2 - |\overline{\mathbf{S}}|^2], \tag{5}$$

where $\overline{\mathbf{S}} = \frac{1}{2}[\nabla\mathbf{U} + (\nabla\mathbf{U})^T]$ is the rate-of-strain tensor and $\overline{\mathbf{\Omega}} = \frac{1}{2}[\nabla\mathbf{U} - (\nabla\mathbf{U})^T]$ is the spin tensor and describes the rate-of-rotation. In regions where $Q_{crit} > 0$, the dynamics of the flow is dominated by rotations, and in regions where the rate-of-strain is higher than the rate-of-rotation, we have $Q_{crit} < 0$. The first two columns of Fig. 14 show the Q_{crit} and the horizontal velocity (first column) and magnetic field (second column). Although only three M-vortices are shown, they represent the general tendency for type I and type II M-vortices. We see that the flow dynamics in the region where the magnetic field continuously curls is mainly described by the rate-of-strain of the flow. For a type I M-vortex which intersects a K-vortex (see Fig. 14(a)), even part of the curls occur in a region dominated by the rate-of-strain tensor. The trace of the rate-of-strain tensor, $\overline{\mathbf{S}}$, expresses strain due to compressibility effects, $\nabla\cdot\mathbf{U}$. We can use the trace to decompose the tensor into an isotropic part and a deviatoric part. The isotropic tensor accounts for the strain generated by compressibility effects. In the deviatoric component, $\overline{\mathbf{S}}^d = \overline{\mathbf{S}} - \frac{1}{3}\overline{\mathbf{I}}(\nabla\cdot\mathbf{U})$, there is no trace and it accounts for strain due to shear. One can write the rate-of-strain tensor as,

$$\overline{\mathbf{S}} = \frac{1}{3}\overline{\mathbf{I}}(\nabla\cdot\mathbf{U}) + \overline{\mathbf{S}}^d, \tag{6}$$

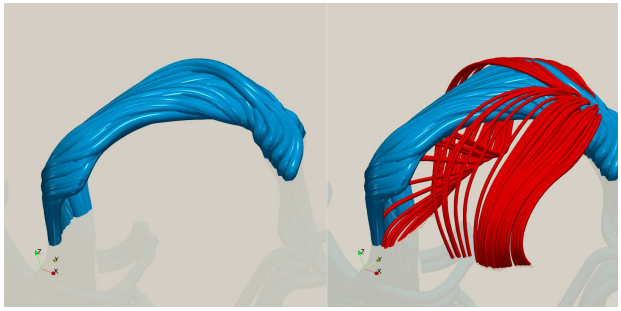

(a)

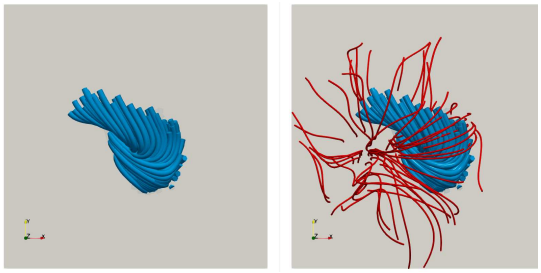

(b)

Figure 13. Left panels: an example of a type II M-vortex where the magnetic field lines are displayed in blue and are traced from random points within the M-vortex boundary, radius ~ 60. . Right panels: M-vortex magnetic field lines (blue) and the velocity field lines (red) surrounding the M-vortex. In both panels the xy-plane is placed at $z = 1$ Mm.

where the first term is an isotropic tensor that accounts for the compressibility and the second term is a deviatoric component of the strain generated by shear.

The compressibility effects in the magnetic field evolution in a M-vortex can be evaluated based on the induction equation, which in the absence of viscosity effects can be decomposed in a way similar to the vorticity equation (Shelyag et al. 2011) as

$$\frac{\partial \mathbf{B}}{\partial t} = \underbrace{(\mathbf{B}\cdot\nabla)\mathbf{U}}_{\text{T1}} - \underbrace{(\mathbf{U}\cdot\nabla)\mathbf{B}}_{\text{T2}} - \underbrace{\mathbf{B}(\nabla\cdot\mathbf{U})}_{\text{T3}}. \tag{7}$$

The term T1 describes the stretching or tilting effects of the magnetic field due to the velocity gradients. Term T2 accounts for the advection of magnetic field lines and the compression effects would be described by term T3. In Fig. 15, we compare the horizontal components of the terms, $T1_h$, $T2_h$ and $T3_h$, for the evolution of the horizontal magnetic field of the M-vortices previously shown in Fig. 14. The ratio of $|T1_h|/|T2_h|$, Fig. 15(a, d) and (g), indicates that both terms are important to the magnetic field evolution inside the M-vortex, and that the tilting term tends to dominate over advection for most of the vortices. The comparison of $|T3_h|$ and terms $|T1_h|$ and $|T2_h|$, Fig. 15(b),(c),(e),(f),(h), and(i), shows that the dilation effect tends to be the least important for the evolution of the M-vortex compared to the other terms. Therefore, it follows from Eq. 6 that the dynamics of the flow in the region with a curling M-vortex is mostly dominated by strain from shear effects and not by rotation, as previously thought, e.g (Brandt et al. 1988; Kitiashvili et al. 2012b; Yadav et al. 2021).

6. DISCUSSIONS AND CONCLUSIONS

We defined a coherent twisted magnetic flux tube as coherent 3D M-vortex, and we concentrated our analysis in M-vortices with detectable twists in the horizontal planes parallel to the photosphere. The M-vortices were automatically detected using IACD and the d-parameter. The IACD method allowed to precisely define the boundary of the coherent twisted magnetic flux tubes even in the magnetoconvection simulations where the magnetic field lines have a chaotic variety of topologies, confirming the results from Rempel et al. (2019). Therefore, the IACD method proves to be a valuable tool to analyze twisted magnetic flux tubes in a simulated solar atmosphere. Furthermore, as the technique has also been previously found to work on two-dimensional flows (Rempel et al. 2019), future analysis using observational magnetic field data will also be possible.

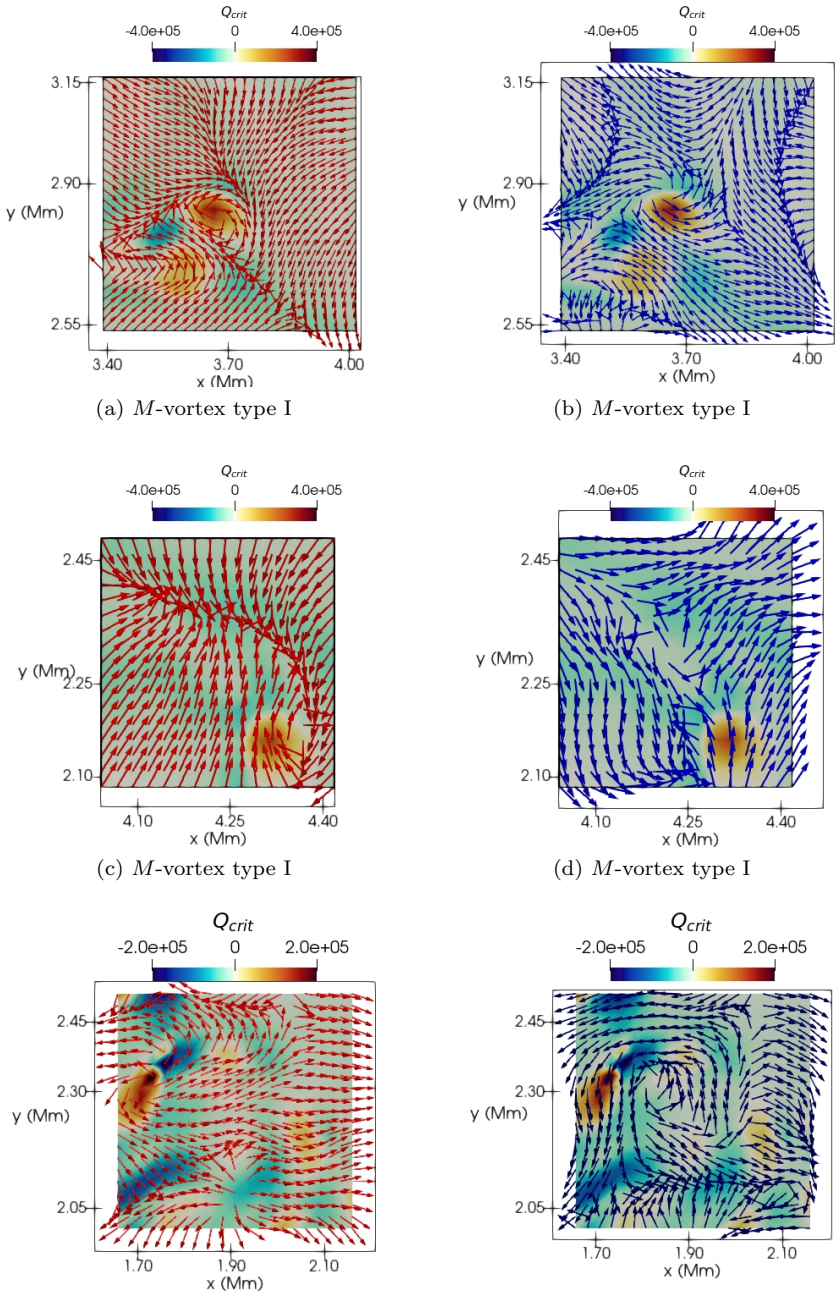

(a) M-vortex type I (b) M-vortex type I

(c) M-vortex type I (d) M-vortex type I

(e) M-vortex type II (f) M-vortex type II

Figure 14. Close view of a region surrounding a M-vortex for a xy-plane placed at the $z = 1.1$ Mm and colored by the Q_{crit}. In (a),(c) and (e) the red arrows indicate the direction of the horizontal velocity field in the plane. In (b),(d) and (f) the blue arrows indicate the direction of the horizontal magnetic field in the plane.

Our results show that both M- and K-vortices are preferentially located in the intergranular downflows. In these regions, we found a transition from an atmospheric flow controlled by gas pressure to a plasma governed by the magnetic field. Moreover, the M- and K-vortices tend to appear in distinct parts of the downflow regions. As expected, the twist of magnetic field lines is observed in parts of the intergranular lanes with the plasma-β close to unity, or in the regions where the plasma flow still may relatively easily change the geometry of the magnetic field lines. The vortical motion in plasma appears in the parts of the atmosphere governed by the magnetic field, in low plasma-β intergranular lanes. The detected M-vortices are outnumbered by K-vortices, resulting from having a smaller total region where the conditions

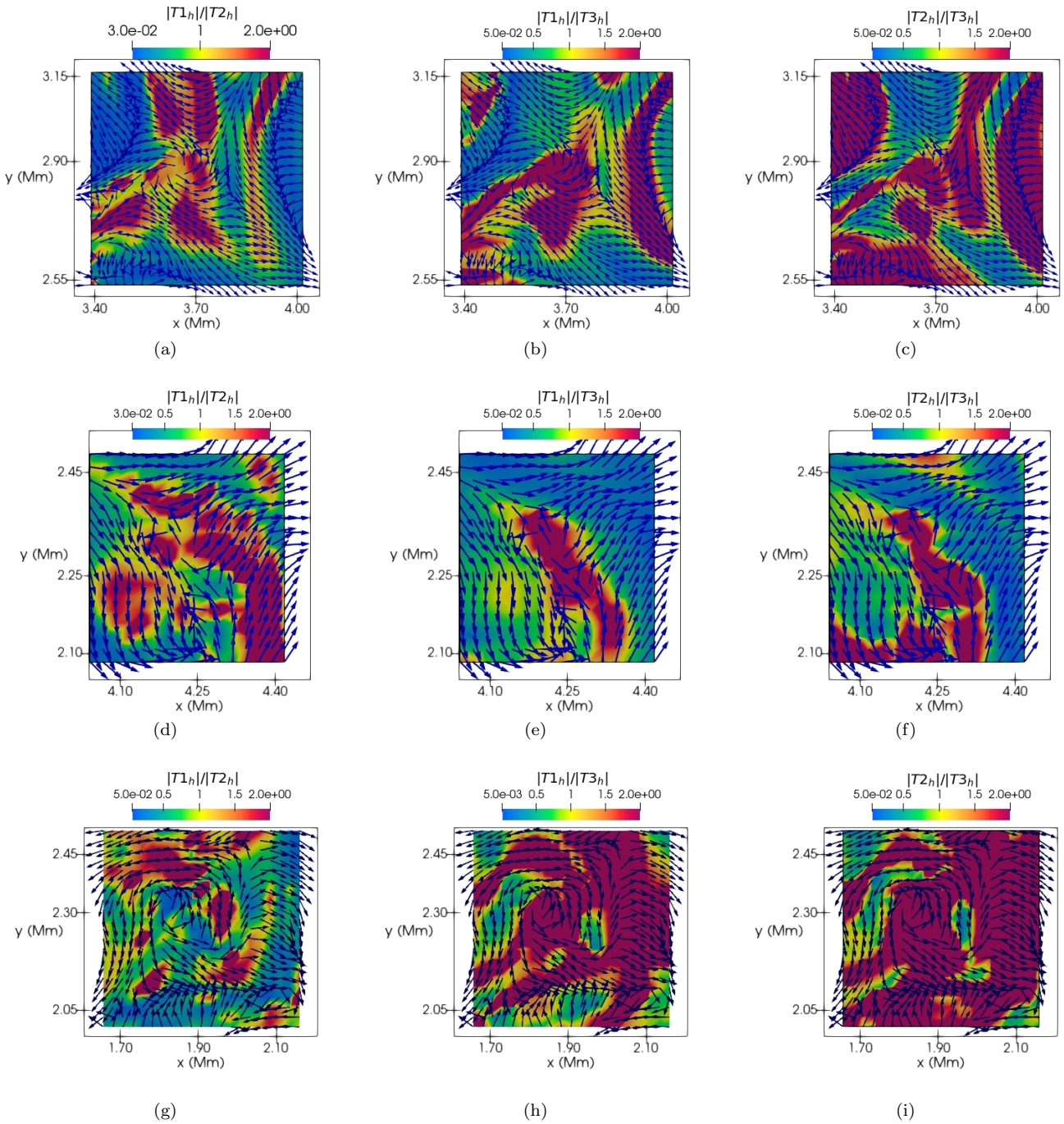

Figure 15. Close view region surrounding an M-vortex for a xy-plane placed at the $z = 1.1$ Mm and colored by: (a),(d),(g) the ratio of terms T1 and T2 defined in Eq.7; (b),(e),(h) the ratio of terms T1 and T3 defined in Eq.7; (c),(f),(i) the ratio of terms T2 and T3 defined in Eq.7

.

for the twist of the lines are met. Thereby, this ratio may differ for other simulations using a different initial magnetic field as, in those cases, we might have larger regions where the plasma β is greater than unity within the downflows interlane. The M-vortices also locally concentrate the vertical magnetic field due to the gas pressure gradient between the vortex boundary and its center, forcing new magnetic field into the M-vortex. Another distinct feature is the high concentration of the vertical current density at the center of the M-vortices, which appears due to the magnetic field's twisting belonging to the structure. The shorter lifetimes may be caused by changes in the flow topology or

the diminution of the plasma-β driven by the M-vortex's magnetic flux accumulation. There are two distinct types of M-vortex present in our simulated solar atmosphere, which show differences between their shape, magnetic and kinetic energy ratio, and preferential plasma regions. The type I M-vortex has a magnetic to kinetic energy ratio larger than unity, and it is mostly a structure aligned along the vertical axis and it presents twisting for a given height range. They appear mostly in regions where the plasma-β is close to unity and the compressibility effects on the plasma dynamics are negligible. The second class of M-vortex was called type II, and it is a magnetic structure with distinct geometry and presenting higher kinetic energy. Type II M-vortices can be found outside downflow regions, where the plasma-β is high and also they tend not to be close to kinetic vortices. The type II vortices appear mostly in regions where the compressibility effects on the plasma are strong. The twist resulting in type I vortices tend to appear in regions of the flow where the magnetic and kinetic energy ratio is already higher than one. Therefore, our findings hint that type I and II vortices are most likely two different entities. Although they have different topologies, both types appear due to the presence of strain in the plasma flow caused by shear flows. The shear twists the magnetic field lines through a given vertical length close to the solar surface in regions where the plasma-β is equal to or larger than unity.

The M-vortices found nearby K-vortices have horizontal field vectors oriented in the opposite direction of the plasma flow, which was also found by Kitiashvili et al. (2013). Furthermore, their centers are never co-spatial with K-vortices. On the other hand, even though the rotational motion from K-vortices do not necessarily generate M-vortices, they can have considerable spatial proximity and even intersect. Therefore, they may exist as a co-depending structure, having a dynamic interplay. Identifying K- and M-vortices as different structures depend on spatial resolution and proper detection methods to define the vortex centers and boundaries. Thus, it is not surprising that misleading conclusions about K-vortices driving twisted magnetic flux tubes have been found in numerical studies, such as Kitiashvili et al. (2013); Iijima & Yokoyama (2017); Yadav et al. (2021). Therefore, further numerical studies together with high-resolution observations at different spatial and temporal scales are essential to correctly describe the interplay between the magnetic field and K-vortices and also the interconnectivity between structures at different height levels. It is worth mentioning that our results do not rule out K-vortices as drivers for MHD waves. Although the K-vortices occur where the magnetic field tension is too high for the rotational motion to significantly twist the magnetic lines, they can still perturb the lines enough to excite waves (see e.g., Moll et al. 2012; Shelyag et al. 2013; Silva et al. 2020). Studies using 2D K-vortices to generate MHD waves in a lower plasma β region were able to perturb the magnetic field lines and drive their torsional motions (Fedun et al. 2011b; Vigeesh et al. 2012), but it was also pointed out that granular buffeting is more efficient for wave generation (Vigeesh et al. 2012). The role of M-vortices in conducting MHD waves and their possible impact on the dynamics of nearby K-vortices are topics to be addressed in future research. Moreover, as M-vortices might arise regardless of kinetic vortices' existence, it is also interesting to further investigate their impact on the solar atmosphere when they appear far from the kinetic structures.

ACKNOWLEDGMENTS

SSAS, VF, GV and ER are grateful to The Royal Society, International Exchanges Scheme, collaboration with Brazil (IES\R1\191114). VF and GV are grateful to Science and Technology Facilities Council (STFC) grant ST/V000977/1 and to The Royal Society, International Exchanges Scheme, collaboration with Chile (IE170301). VF would like to thank the International Space Science Institute (ISSI) in Bern, Switzerland, for the hospitality provided to the members of the team on 'The Nature and Physics of Vortex Flows in Solar Plasmas'. E.L.R. acknowledges Brazilian agencies CAPES, CNPq,and FAPESP (Grants No. 88881.309066/2018-01, No 304449/2017-2 and No. 16/24970-7) for their financial support. This research has also received financial support from the European Union's Horizon 2020 research and innovation program under grant agreement No. 824135 (SOLARNET). This study was financed in part by the Coordenação de Aperfeiçoamento de Pessoal de Nível Superior – Brasil (CAPES) – Finance Code 88882.316962/2019-01. This research was undertaken with the assistance of resources and services from the National Computational Infrastructure (NCI), which is supported by the Australian Government.

REFERENCES

Balmaceda, L., Vargas Domínguez, S., Palacios, J., Cabello, I., & Domingo, V. 2010, A&A, 513, L6, doi: 10.1051/0004-6361/200913584

Bonet, J. A., Márquez, I., Almeida, J. S., Cabello, I., & Domingo, V. 2008, ApJL, 687, L131. http://stacks.iop.org/1538-4357/687/i=2/a=L131

Bonet, J. A., Márquez, I., Almeida, J. S., et al. 2010, ApJL, 723, L139. http://stacks.iop.org/2041-8205/723/i=2/a=L139

Brandt, P. N., Scharmert, G. B., Ferguson, S., et al. 1988, Nature, 335, 238, doi: 10.1038/335238a0

Chian, A. C.-L., Silva, S. S. A., Rempel, E. L., et al. 2019, MNRAS, 488, 3076, doi: 10.1093/mnras/stz1909

Ebadi, H., Shahmorad, S., & Vasheghani Farahani, S. 2021, Monthly Notices of the Royal Astronomical Society, 502, 4930, doi: 10.1093/mnras/stab334

Fedun, V., Shelyag, S., Verth, G., Mathioudakis, M., & Erdélyi, R. 2011a, Annales Geophysicae, 29, 1029, doi: 10.5194/angeo-29-1029-2011

Fedun, V., Verth, G., Jess, D. B., & Erdélyi, R. 2011b, The Astrophysical Journal, 740, L46, doi: 10.1088/2041-8205/740/2/l46

Haller, G., Hadjighasem, A., Farazmand, M., & Huhn, F. 2016, JFM, 795, 136, doi: 10.1017/jfm.2016.151

Iijima, H., & Yokoyama, T. 2017, The Astrophysical Journal, 848, 38, doi: 10.3847/1538-4357/aa8ad1

Kato, Y., & Wedemeyer, S. 2017, A&A, 601, A135, doi: 10.1051/0004-6361/201630082

Kitiashvili, I. N., Kosovichev, A. G., Lele, S. K., Mansour, N. N., & Wray, A. A. 2013, ApJ, 770, 37. http://stacks.iop.org/0004-637X/770/i=1/a=37

Kitiashvili, I. N., Kosovichev, A. G., Mansour, N. N., Lele, S. K., & Wray, A. A. 2012a, Physica Scripta, 86, 018403, doi: 10.1088/0031-8949/86/01/018403

Kitiashvili, I. N., Kosovichev, A. G., Mansour, N. N., & Wray, A. A. 2012b, The Astrophysical Journal, 751, L21, doi: 10.1088/2041-8205/751/1/l21

Moll, R., Cameron, R. H., & Schüssler, M. 2012, A&A, 541, A68, doi: 10.1051/0004-6361/201218866

Mumford, S. J., Fedun, V., & Erdélyi, R. 2015, The Astrophysical Journal, 799, 6, doi: 10.1088/0004-637x/799/1/6

Rempel, E. L., Chian, A. C.-L., Beron-Vera, F. J., Szanyi, S., & Haller, G. 2017, MNRASL, 466, L108, doi: 10.1093/mnrasl/slw248

Rempel, E. L., Gomes, T. F. P., Silva, S. S. A., & Chian, A. C.-L. 2019, Phys. Rev. E, 99, 043206, doi: 10.1103/PhysRevE.99.043206

Requerey, I. S., Cobo, B. R., Gošić, M., & Bellot Rubio, L. R. 2018, A&A, 610, A84, doi: 10.1051/0004-6361/201731842

Shelyag, S., Cally, P. S., Reid, A., & Mathioudakis, M. 2013, The Astrophysical Journal, 776, L4, doi: 10.1088/2041-8205/776/1/l4

Shelyag, S., Cally, P. S., Reid, A., & Mathioudakis, M. 2013, ApJL, 776, L4, doi: 10.1088/2041-8205/776/1/L4

Shelyag, S., Keys, P., Mathioudakis, M., & Keenan, F. P. 2011, A&A, 526, A5, doi: 10.1051/0004-6361/201015645

Shelyag, S., Mathioudakis, M., & Keenan, F. P. 2012, ApJL, 753, L22. http://stacks.iop.org/2041-8205/753/i=1/a=L22

Shetye, J., Verwichte, E., Stangalini, M., et al. 2019, The Astrophysical Journal, 881, 83, doi: 10.3847/1538-4357/ab2bf9

Silva, S. S. A., Fedun, V., Verth, G., Rempel, E. L., & Shelyag, S. 2020, The Astrophysical Journal, 898, 137, doi: 10.3847/1538-4357/ab99a9

Silva, S. S. A., Rempel, E. L., Gomes, T. F. P., Requerey, I. S., & Chian, A. C.-L. 2018, The Astrophysical Journal, 863, L2, doi: 10.3847/2041-8213/aad180

Snow, B., Fedun, V., Gent, F. A., Verth, G., & Erdélyi, R. 2018, The Astrophysical Journal, 857, 125, doi: 10.3847/1538-4357/aab7f7

Tziotziou, K., Tsiropoula, G., & Kontogiannis, I. 2019, A&A, 623, A160, doi: 10.1051/0004-6361/201834679

Tziotziou, K., Tsiropoula, G., & Kontogiannis, I. 2020, A&A, 643, A166, doi: 10.1051/0004-6361/202038951

Tziotziou, K., Tsiropoula, G., Kontogiannis, I., Scullion, E., & Doyle, J. G. 2018, A&A, 618, A51, doi: 10.1051/0004-6361/201833101

Vasheghani Farahani, S., Ghanbari, E., Ghaffari, G., & Safari, H. 2017, A&A, 599, A19, doi: 10.1051/0004-6361/201629563

Vigeesh, G., Fedun, V., Hasan, S. S., & Erdélyi, R. 2012, The Astrophysical Journal, 755, 18, doi: 10.1088/0004-637x/755/1/18

Vögler, A., Shelyag, S., Schüssler, M., et al. 2005, A&A, 429, 335, doi: 10.1051/0004-6361:20041507

Wedemeyer-Böhm, S., & Rouppe van der Voort, L. 2009, A&A, 507, L9, doi: 10.1051/0004-6361/200913380

Wedemeyer-Böhm, S., Scullion, E., Steiner, O., et al. 2012, Nature, 486, 505, doi: 10.1038/nature11202

Yadav, N., Cameron, R. H., & Solanki, S. K. 2021, A&A, 645, A3, doi: 10.1051/0004-6361/202038965